Electronic Supplementary Material (ESI) for New Journal of Chemistry.

Supporting Information

Mechano-Bactericidal Interactions of Nanoclay-Bacteria for Inhibiting Inflammatory Response to Enhance Wound Healing

Dongyue Wang,[a] Aidong Tang,[b,c,d] Huaming Yang [a,b,c,d*]

[a] *Hunan Key Laboratory of Mineral Materials and Application, School of Minerals Processing and Bioengineering, Central South University, Changsha 410083, China*

[b] *Engineering Research Center of Nano-Geomaterials of Ministry of Education, China University of Geosciences, Wuhan 430074, China.*

[c] *Faculty of Materials Science and Chemistry, China University of Geosciences, Wuhan 430074, China*

[d] *Key Laboratory of Functional Geomaterials in China Nonmetallic Minerals Industry, China University of Geosciences, Wuhan 430074, China*

[*] Correspondence: hmyang@csu.edu.cn, hm.yang@cug.edu.cn (H. Yang)

Table of contents

Supplementary Tables

Experimental section

Materials

Medical grade kaolinite was obtained from Aladdin Industrial Corporation, Shanghai, China. The detailed process of concocting based on Chinese Medicine is that kaolinite was calcined under 300 °C, 400 °C and 500 °C for 1 h. In detail, 1 g of kaolinite is placed in a crucible and then placed in a muffle furnace. The heating rate is 10 °C/min and the holding time is 1 hour when the temperature reaches the setting temperature 300 °C, 400 °C and 500 °C. The calcined samples were labeled as Kaol300, Kaol400 and Kaol500, respectively.

Interaction force Calculation

The mechanical interaction between kaolinite and bacteria are determined by long-range forces. Therefore, accurately determining the long-range forces between bacterial cell and kaolinite samples leads to a basic understanding of mechanical-bacteriacidal mechanism[1, 2]. To gain more insight into the mechanical interaction, DLVO theory is used to calculate vder Waals forces, and repulsive electrostatic forecs and the total interaction energy. The Van der Waals attractive energy for cell-Kaol can be calculated as:

$$V_{vdW} = -\frac{A_{132}}{6H}\frac{R_1R_2}{(R_1R_2)} \tag{1}$$

Where H is the interactional distance, and R_1 and R_2 are the radius of samples and bacterial cell, respectively. A_{132} is the Hamaker constant of kaolinite samples and bacteria system. The Hamaker constant is calculated according to the equations as:

$$A_{132} = A^0_{132} + A^{\xi}_{132} \tag{2}$$

$$A^0_{132} = \frac{3}{4}\kappa \mathrm{T}\left(\frac{\varepsilon_1 - \varepsilon_3}{\varepsilon_1 + \varepsilon_3}\right)\left(\frac{\varepsilon_2 - \varepsilon_3}{\varepsilon_2 + \varepsilon_3}\right) \tag{3}$$

$$A^{\xi}_{132} = \frac{3h\nu_e}{8\sqrt{2}}\frac{(n_1^2 - n_3^2)(n_2^2 - n_3^2)}{(n_1^2 + n_3^2)^{1/2}(n_2^2 + n_3^2)^{1/2}[(n_1^2 + n_3^2)^{1/2} + (n_2^2 + n_3^2)^{1/2}]} \tag{4}$$

where A^0_{132} is the total contribution of orientation force and induction force to van der Waals force, A^{ξ}_{132} is the contribution of the London dispersion forces; κ is the Boltzmann constant; T is the temperature; n_1 and n_2 are refractive index of kaolinite and bacteria, respectively; n_3 is the refractive index of water; ε_1 and ε_2 are dielectric constants of kaolinite and bacteria, respectively; ε_3 is the refractive index of water; h is Planck's constant; and ν_e is the dominant electron absorption frequency of ultraviolet light.

The repulsive electrostatic energy was calculated from:

$$V_E = \pi\varepsilon_a\frac{R_1R_2}{R_1 + R_2}(\psi_1^2 + \psi_2^2)\{\frac{2\psi_1\psi_2}{\psi_1^2 + \psi_2^2}\ln\left[\frac{1 + \exp(-\kappa H)}{1 + \exp(-\kappa H)}\right] + \ln[1\text{-}\exp(-2\kappa H)]\} \tag{5}$$

Here, ψ_1 and ψ_2 are the surface potentials of kaolinite and bacteria, respectively. The ζ values were used as the surface potentials; H is the distance between kaolinite particles and bacteria; and κ^{-1} is the Debye length representing the thickness of double-layer and calculated by Eq. 6 where C_B is the electrolyte concentration.

The parameters for the calculation of DLVO energy curves are shown in Table S1 and Table S2.

Surface free energy calculation

The total surface free energy γ is composed of two parts: the nonpolar part γ^{LW} (i.e., Lifshitz-van der Waals) and the polar part γ^{AB} (i.e., Lewis acid-base) according to the van Oss-Chaudhury-Good theory[3]. The non-polar dispersive component is mainly attributed to London forces, while the polar component (Lewis acid-base interactions) is mainly associated with hydrogen bonding and the behavior of the electron donor-acceptor (i.e., γ^- and γ^+). The surface free energy of the solid γ_S and the liquid γ_L can be calculated as:

$$\gamma_s = \gamma_s^{LW} + \gamma_s^{AB} = \gamma_s^{LW} + 2\sqrt{\gamma_s^+ \gamma_s^-} \tag{6}$$

$$\gamma_L = \gamma_L^{LW} + \gamma_L^{AB} = \gamma_L^{LW} + 2\sqrt{\gamma_L^+ \gamma_L^-} \tag{7}$$

According to the Dupre equation, the solid-liquid interfacial free energy γ_{SL} is expressed as:

$$\gamma_{SL} = \gamma_S + \gamma_L - 2(\sqrt{\gamma_S^{LW} \gamma_L^{LW}} + \sqrt{\gamma_S^+ \gamma_L^-} + \sqrt{\gamma_S^- \gamma_L^+}) \tag{8}$$

By combining Eqs. (6), (7), and (8), and Young's equation, Eq. (9) is obtained

$$(\gamma_L^{LW} + 2\sqrt{\gamma_L^+ \gamma_L^-})(1+\cos\theta) = 2(\sqrt{\gamma_S^{LW} \gamma_L^{LW}} + \sqrt{\gamma_S^+ \gamma_L^-} + \sqrt{\gamma_S^- \gamma_L^+}) \tag{9}$$

Based on Eq. (4), the solid surface energy and its components can be obtained by measuring the contact angles of three different liquids (two polar liquids are required).

$$\Delta G_{sl} = \Delta G_{sl}^{LW} + \Delta G_{sl}^{AB} = -2\sqrt{\gamma_s^{LW}\gamma_l^{LW}} - 2\sqrt{\gamma_s^+\gamma_l^-} - 2\sqrt{\gamma_s^-\gamma_l^+} \tag{10}$$

Where the interfacial interaction free energy ΔG_{SL} between solid and liquid can be divided into two parts: the first component results from the non-covalent Lifshitz–van der Waals free energy ΔG_{LW} and the second component are from the Lewis acid–base free energy ΔG_{AB}. The contact angles and physical parameters of different liquids are shown in Table S3 and Table S4.

Adhesion experiments

The incubated bacteria were separated from the culture medium in the late exponential growth phase. The isothermal adhesion curve of bacteria to kaolinite particles was performed in 1mM KCl solution at pH 7.0, The separated cells were washed three times by centrifugation with sterilized distilled-deionized water. The bacterial cells were then resuspended to obtain different concentrations of bacterial suspension with a dry biomass concentration ranging from 10~1842 mg bacteria L^{-1}. The 0.1 g concocted kaolinite was added to 20 mL of the different concentrations of bacteria. The mixture was shaken at 37 °C and 150 rpm for 2 h. Then, 2 mL of sucrose solution (60% by weight) was injected into the mixture to separate the un-adhered bacteria from those attached to samples. After injection of sucrose solution, the suspension was centrifuged at 3200 g for 20 min. The suspension of the un-adhered bacterial cells was determined directly by a spectrophotometer at a wavelength of 600 nm. The standard curve for different concentrations of bacteria was determined accordingly. The adhesion data conformed to the Freundlich equation:

$$C_S = K_f \cdot C^{1/n} \tag{11}$$

where *C*s ((mg bacterial) (g Kaol) $^{-1}$) is the bacterial concentration adhered onto kaolinite particles, C ((mg

bacterial) (L) $^{-1}$) is the bacterial concentration in equilibrium solution, K_f is the coefficient related to adhesion capacity, and 1/n stands for the linearity exponent.

Atomic force microscopy (AFM) tests

The cells were modified on the tip of the probe, and the powder sample was pressed and put into the AFM (Agilent 5500) liquid stage. The liquid was placed into the sweeping area after settling in pure water for 1 h. Silicon nitride tips with a nominal spring constant of 0.32 N/m were used to obtain both images and collect cellular force data. Silicon nitride tips with a nominal spring constant of 0.32 N/m were used for the images and cellular force data. The spring constants (κ_{cell}) were determined from the slope of the extension curve using the equation below:

$$1/\kappa_{effective} = 1/\kappa_{cell} + 1/\kappa_{cnatilever} \quad (11)$$

Small-angle neutron scattering (SANS) measurements

Small angle neutron scattering measurements were performed on the time-of-flight (TOF) Small-Angle Neutron Spectrometer at China Spallation Neutron Source (SANS@CSNS), Dongguan, China. It utilizes beam port of the CSNS target station facing a coupled liquid hydrogen moderator and adopts a short straight beamline configuration with the classic point-focusing pin-hole camera geometry[4, 5]. The sample was loaded in 1.0 mm thick cell (Hellma, Germany) and the small angle neutron scattering data were collected at room temperature with wavelength band from 1.4 to 8.5 Å. The scattering intensity of the empty beam and the cell were subtracted. In order to investigate the effect of the interfacial interaction on the bacterial membrane, especially for the hydrogen bonding interaction, the small-angle neutro scattering (SANS) was used to study the structure of bacterial membrane treated with samples. The cell membrane structure can be characterised by SANS in their native and hydrated state. Moreover, SANS supply an efficient approach to determin the nanoscle size of the cell structure range from 1 nm to several hundreds nm[4, 5]. The 3-strip model based on the SANS dates can supply an efficient approach to evaluate the important parameters of the cell membrane structure, such as the thickness of the bilayer. The fitted parameters from the model have proven to be hgihly successful and consistent with the privious experiment resuts. It indicates the model can elucidate the cell membrane properties and provide theoretical caculations at the molecular level[40,41]. The scattering intensity based on the 3-strip model can be expressed as:

$$I = [2D_C(\rho_C-\rho_{CH})\sin(qD_C) + 2(D_C+D_H)(\rho_H-\rho_{Water})\sin(q(D_C+D_H))]^2 \quad (13)$$

where sinc(x)=sin(x)/x; D_H, D_C are the thickness of headgroup and hydrocarbon thickness, respectively. ρ_H and ρ_C are scattering length densities (NSLDS) of lipid bilayer´s hydrocarbon, headgroup, respectively; ρ_{water} is scattering length densities of the buk water.

Proteomics experiments

The bacteria cells were harvested after incubation. In brief, the supernatants were centrifuged at 300 g for 10 min, 2000 g for 20 min, and 10000 g for 30 min to remove large membrane fragments. Finally, the supernatants were centrifuged at 100 000 g for 70 min to obtain exosomes. Each sample was measured three times using Nanosight automatic analysis settings. The isolated exosomes were fixed and examined by transmission electron microscopy (Hitachi, Tokyo, Japan). Particle size and concentration distribution of exosomes were measured using NTA (Malvern Instruments, Malvern, UK). The protein samples were

resolved by 10% SDS-PAGE and stained with Coomassie Brilliant Blue R250 in parallel. The full lanes were cut into small bands. The peptides were then resuspended in 0.1% formic acid and analyzed using an ultraperformance LC−MS/ MS platform. All data were expressed as mean ± standard deviation. For statistical analysis, a two-tailed Student's t test was utilized and performed using ANOVA analyses. The gene ontology (GO) analysis was done with Blast 2, and Kyoto Encyclopedia of Genes and Genomes (KEGG) pathway analysis was performed using KAAS (KEGG Automatic Annotation Server) software. The Fisher's exact test allowed comparing distribution of GO classification or KEGG pathway. To simultaneously classify the two dimensions of sample and protein expression, cluster analysis was performed using Cluster 3.0 software. Overall, all data were analyzed and ranked by p-value (hypergeometric test), and statistical p-values of <0.05 were considered significant.

Antibacterial activity

The antibacterial activity of samples was assessed with Gram-negative (E. coli., ATCC 25922) bacteria by the colony count method. 0.1 g sample powders were added into 10 mL Luria-Bertani broth (LB), then well mixed with 100 μL bacteria dilutions (about $10^{5\sim6}$ CFU/mL). The mixture was incubated under constant shaking at 37 °C, 220 rpm for 4 h. 50 μL of each dilution was dispersed onto LB agar plates. Colonies on the plates were counted after incubation at 37 °C for 16 h.

Morphological observation of bacteria

A glutaraldehyde solution (2.5%) was used to fix the bacteria overnight, and the samples were dehydrated with ethanol solutions (30, 50, 75, 90, 95, and 100%) sequentially and vacuum-dried. The morphological images of the bacteria were acquired by SEM and TEM. Each group contained three parallel samples and at least two sets of images were acquired from each sample.

Live/dead bacterial staining assay

Calcein AM/PI double stain kit was used. Here, 20 μL of frozen *E. coli* was added to 20 mL LB medium for 15 h, and then incubated with 0.1 g powder sample at 37 °C and shaken at 150 rpm for 15 h. After centrifugation at 3000 rpm for 5 min, the supernatant was removed, and the bacterial precipitates were washed with PBS three times. Calcein AM/PI (5 μL) was added to the bacterial suspension (200 μL) and incubated in the dark at 150 rpm for 15 min. The samples were imaged with a fluorescence microscope (Olympus FV1200).

In vivo uninfected/infected wound healing assay

The wound-healing efficacy of the samples was evaluated in male SPF ICR rats weighing 250-300 g. All rats were randomly divided into 5 groups: the uninfected, Kaol, Kaol300, Kaol400, and Kaol500. Each group contained 14 rats. The rats were anaesthetized by 10% chloral hydrate (30 mg/kg), and one full-thickness round skin wounds (1 cm diameter) were created on the dorsum of each rat. 100 μL of *E. coli* suspension (1.0×10^8 CFU/mL) was applied to create infected wounds, and 100 μL of sterile physiological saline was applied to the wounds of the uninfected groups. The wounds became severely infected by 48 h after the addition of the bacterial suspensions. The wound size was measured with Vernier calipers on the 3 th, 5 th, 7 th, 10 th, and 14 th day. The wound closure rate was calculated as follows: wound closure rate (%) = (original wound area - wound area at test time)/original wound area ×100%. The mice were

sacrificed, and the wound tissues were fixed in formalin for paraffin sections. Sirius red and Masson staining were completed, and the samples were then observed and photographed.

Statistical analysis

Statistical analysis was carried out using SPSS 9.0 software, and all data were presented as means ± standard deviation (SD). The statistical significance was obtained by one-way ANOVA with Tukey's post hoc test. The differences were considered to be statistically significant for a p-value <0.05 (*P < 0.05, **P < 0.01, ***P < 0.001).

Characterization

Powder X-ray diffraction (XRD) measurements were recorded on a Bruker D8 Advance operating at 40 mA and 40 kV with Cu Kα radiation. TGA used a STA449C instrument at an airflow of 60 mL/min and a heating rate of 5 °C/min. Fourier transform infrared (FTIR) analysis of the samples was conducted with a FTIR spectrophotometer (Scientific Nicolet 6700) between 4000 and 400 cm^{-1}. SEM images were taken on a JEOL JSM-7001F field emission scanning electron microscope. HRTEM images were obtained on EM-ARM300F electron microscope. The UV–vis absorption spectra were recorded on a PE, Lambda1050 UV–vis spectrophotometer.

Supplementary Results

Characterization

X-ray diffraction (XRD) results showed sharp characteristic peaks at 12.3 ° and 25 ° (Fig. S1a), which are due to the (001) and (002) crystal planes of kaolinite, respectively (JCPDS card no.14-0164). Thermogravimetry–differential scanning (TG-DSC) was used to analyze the thermal properties of raw kaolinite. The weight loss of kaolinite was 0.98% at 200 °C, which indicates that the moisture content was removed (Fig. S1b). The weight loss increased to 13.37 % at higher temperatures, suggesting that the hydroxyl groups were largely removed from kaolinite. Based on the DSC analysis, the endothermic and exothermic peaks were 527 °C and 994 °C respectively, which indicates that dehydroxylation occurs between 200 °C and 527 °C, which agreed with the TG-DSC analysis (Fig. S1b). Furthermore, the crystal structure of kaolinite was not changed when concocted between 200 °C and 527 °C. SEM images demonstrated that kaolinite concocted at 400 °C is much looser and slice-layered versus those concocted at other temperatures (Fig. S2). The XRD patterns implied that calcination between 200 °C and 527 °C does not change the crystal structure of kaolinite (Fig. S3a). With increasing calcination temperature, the bending vibration peak of −OH at 3660 cm^{-1} gradually became flat, illustrating that calcination could remove hydroxyl groups from kaolinite (Fig. S3b). Moreover, the zeta potential of the samples changed from 24.90 mV to 20.73 mV and then decreased to -22.70 mV (Table S1). The size of the samples increased from 0.58 μm to 0.83 μm with calcination temperature increasing. There was a decrease to 0.63 μm at 400 °C, the size of the samples increased to 0.13 μm above 400 °C (Table S1). The characteristic physicochemical changes of kaolinite were mainly due to the dihydroxylation from calcination while not changing the crystal structure. Thus, the physicochemical properties of the kaolinite surface were responsible for the antibacterial activities.

DLVO analysis

The antibacterial activity was affected by contact kill mechanism for 2D materials. The first step involves bacterial adhesion onto the materials. Long-range interactions control the first step via electrostatic forces and van der Waals forces. These forces determine whether the materials can reach sufficiently close to the surface of bacteria such that the first step could occur[1, 6]. Thus, long-range interactions between samples and bacteria play important roles in antibacterial activity. The long-range interactions are described by Derjaguin–Landau–Verwey–Overbeek (DLVO) theory, which was used to clarify the interaction process and provide greater insight into the calcination strategies relative to long-range interactions in the antibacterial mechanism. DLVO theory was used to calculate van der Waals, electrostatic interactions, and the total interaction energy. The total interaction energy is the sum of the electrostatic and van der Waals attractive energy. The attractive electrostatic force attributed to the positive edge may be weaker than the pulsive force. The hydrophobic force is not responsible for the overall interactions between kaolinite samples and the bacterial cell across the long-distance because the force decreased exponentially with decreasing distance. Thus, the hydrophobic force could not drastically affect the interaction energy trend. The interfacial interactions between bacteria and kaolinite samples could also be improved through non-DLVO forces such as hydrogen bonding. Hydrogen bonds are governing factor that mediates the attachment of bacteria onto mineral surface. Thus, non-DLVO forces such as hydrogen bonds play an important role in attachment and antibacterial activity. Bacteria firstly adhere to the material surface, resulting in direct contact between bacterium and material. The material induces membrane stress, resulting in a disturbed cell membrane. To study the effect of these interactions, equilibrium adhesion isotherms of *E. coli* to calcined kaolinite samples were investigated because the adhesion plays an important role during the direct interactions. The total interaction energy barrier between samples of Kaol400 is the lowest compared to other samples, indicating Kaol400 could interact with bacteria through long-distance forces (Fig. S4).

Surface free energy analysis

The essays will focus on hydrogen bonding formation, which is associated with the Lifshitz–van der Waals and Lewis acid-base theories. The interfacial interactions between bacterial cells and kaolinite samples are affected by their surface properties and are determined by the substrate surface free energy. Several intermolecular interactions including hydrogen bonding are involved in the interfacial interactions between bacterial cells and kaolinite samples[7, 8]. Therefore, accurately determining the surface free energy of concocted Kaol leads to a basic understanding of interfacial interactions between bacteria and concocted kaolinite samples. Van Oss–Chaudhury–Good theory was used to calculate surface free energy to investigate the interfacial interactions. Here, the total surface free energy γ is composed of two parts: the nonpolar part γ^{LW} (Lifshitz–van der Waals) and the polar part γ^{AB} (Lewis acid-base interactions). The non-polar component is mainly attributed to the London force, the orientation force, the induction force, and the dispersion force. The polar component (Lewis acid–base interactions) is due to hydrogen bonding and divided into two parts: the electron donor (γ^-) and the electron acceptor (γ^+). The surface free energy parameters of three liquids used to determine surface free energy of kaolinite samples are shown in Table S3 and Fig. S5. Fig. S6 illustrates the concocting strategy that could regulate surface free energy. Lewis

acid component of Kaol400 is the highest representing Kaol400 exhibits the strongest electron-accepting ability which contribute to forming hydrogen bonds (Fig. S6a). The Lewis base component of Kaol350 and Kaol400 is lower than other samples indicating the Lewis base component plays a little important role in the interactions. As the calcination temperature increased to 500 °C, the γ^{LW} decreased from 41 mJ/m^2 to 39 mJ/m^2 and then increased to about 43 mJ/m^2. Lifshitz–van der Waals free energy γ^{LW} of Kaol400 is lower compared with other samples indicating Lifshitz–van der Waals free energy could not contribute to improving the interactions between Kaol400 and bacteria (Fig. S6b). However, the total free energy has a similar trend with the polar part γ^{AB}, indicating the polar interactions are dominant in the interfacial interactions (Fig. S6c). The adhesion work between samples and bacteria indicates that Kaol400 needs smaller energy to interact with bacteria (Fig. S6d). Therefore, the polar component plays a dominant role in the total interaction energy and significantly affects the interfacial interactions between bacteria and kaolinite samples. Higher Lewis acid-base pairing leads to stronger hydrogen bonding interactions. The formation capacity of hydrogen bonding between bacteria and Kaol400 was much stronger.

Adhesion experiment analysis

The batch equilibrium experimental data and the fitted parameters for the kaolinite samples show that the K_f values of concocted kaolinite samples increased with increasing temperature until 400 °C, and then decreased with calcination temperature increases (Fig. S7&8). The K_f value of Kaol400 was the highest and was about 11 times as large as raw kaolinite. These results indicate that Kaol400 has good adhesion capacity and could adhere to the bacteria surface more quickly. The adhesion capacity of the samples exhibits a similar trend and is consistent with the DLVO interactions energy barriers and surface free energy. Thus, the adhesion capacity can be remarkably improved by reducing the DLVO energy barriers and enhancing the surface free energy especially polar interaction. Increased adhesion capacity could be achieved by adjusting the interactions via the physicochemical properties during calcination. We suggest that the interactions not only affect the adhesion but also the antibacterial activity mechanism.

AFM analysis

AFM can be used as a probe to measure the biophysics of cells. The tip can be gently pushed into the cell and retracted to directly investigate kaolinite interaction forces with the outer membrane[9, 10]. The cantilever was immobilized by bacteria (Fig. S9a). The approach curves of Kaol400 have higher attractive forces with 862 pN than Kaol with 181 pN (Fig. S9b). During the retraction, the interaction forces between Kaol400 and bacteria are 4.7 nN higher than the forces between Kaol and bacteria, which is consistent with the DLVO theory and surface free energy theory. The interaction force and energy of the bacteria on Kaol surface were also analyzed (Fig. S9c&d). The surface of Kaol400 exhibited stronger force and lower interaction energy to overcome the energy barrier, indicating that Kaol400 can interact with bacteria, which could result in membrane changes via interactions. Therefore, the stronger interactions of bacteria with Kaol400 represent irreversible adhesion and is sufficient for bacteria to bind irreversibly to kaolinite surfaces. To further study the integrity and changes in the bacterial membrane, extension and retraction curves acquired from AFM force measurements can provide changes of the biophysical properties of bacteria treated with kaolinite samples. The bacteria stiffness from the linear compression region was

calculated according to Equation 12. $K_{effective}$ was calculated from the slope of this regime. The *k* cantilever is the spring constant of the AFM cantilever. The cellular spring constant *k*cell was determined from the linear slope of the extension curve. The bacteria turgor pressure generated from interactions between bacteria and Kaol is directly related to the cellular spring constant. The kcell values of the bacteria treated by Kaol and Kaol400 are 0.107 and 0.506, respectively, which indicates that the turgor pressure caused by Kaol400 is much higher than that of the bacteria treated by Kaol (Fig. S10).

Analysis of cell membrane disruption

With the bacterial membrane destroyed, cytoplasmic constituents of bacteria such as DNA and RNA are released from cells and can be measured via UV absorption at 260 nm (Fig. S11). The optical density (OD) ratio of a bacterium suspension incubated with Kaol400 shows the highest OD ratio by two-fold higher than other samples. The results agree with the antibacterial activity and interaction measurements and the reflux of DNA and RNA, directly associated with damage to the bacterial membrane resulting from the nano-bio interactions between bacteria and kaolinite samples.

Proteomics analysis

Exosome properties were studied after Kaol treatment, which was utilized to study the membrane structure changes induced by interactions[11, 12]. Fig. S15&16 show the characteristics of exosomes from bacteria and the protein identification data of exosomes from bacteria (Movie S1). Each point in the differential expression volcano map represents a protein. The abscissa represents the logarithm of the differential expression of multiple proteins in two samples, and the ordinate is the negative logarithm of the error detection rate. A higher absolute value of the abscissa implies a greater expression of multiple differences between the two samples; a higher value of the ordinate implies significant differential expression and reliable differential expression protein. The value of the ordinate of the differential expression protein of bacteria treated by Kaol400 is 6; the value of the ordinate of the differential expression protein of Kaol-treated bacteria is only 3.5. Therefore, there are protein expression differences between the two samples. The enrichment factor was used to analyze the enrichment degree of pathways, and Fisher's exact test was used to calculate the significance of enrichment[13, 14]. The abscissa is an enrichment factor representing the proportion of differentially expressed proteins in an annotated pathway to the total number of genes in the pathway. A larger enrichment factor leads to a more significant enrichment level of differentially expressed proteins in this pathway. The ordinate is -log10 (Q value), where the Q value is the p-value after multiple hypothesis test corrections[15]. Therefore, a larger ordinate implies a more reliable enrichment significance for differentially expressed proteins in this pathway that proteins represent. The enrichment factor of the differentially expressed protein in bacteria treated by Kaol400 is significantly higher than those with differential protein expression in bacteria treated by Kaol (Fig. S18). Therefore, the enrichment level of differentially expressed proteins in Kaol400 treated bacteria is higher compared to other samples. The enrichment level of differentially expressed proteins of Kaol400 is more remarkable than that of bacteria treated with Kaol. The enrichment level of differentially expressed proteins from Kaol400 is still significant versus bacteria treated with Kaol.

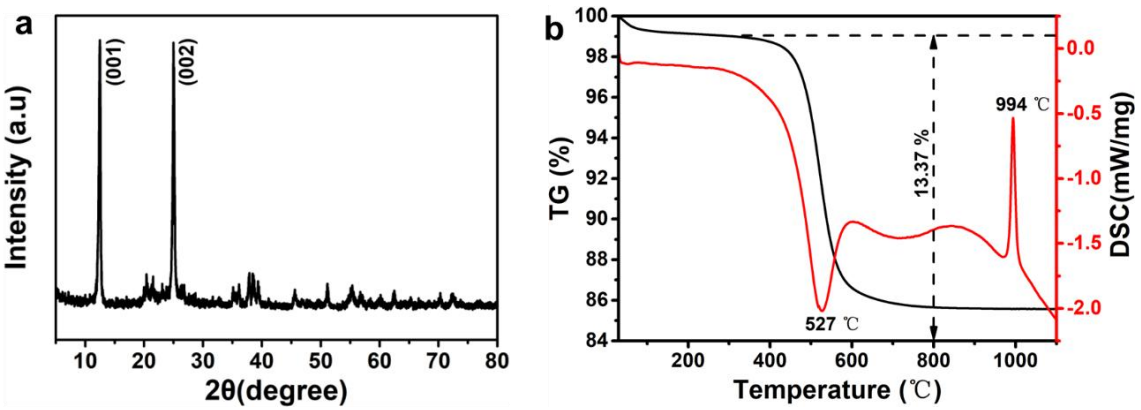

Fig. S1 Characterizations of kaolinite. (a) XRD patterns. (b) TG-DSC analysis.

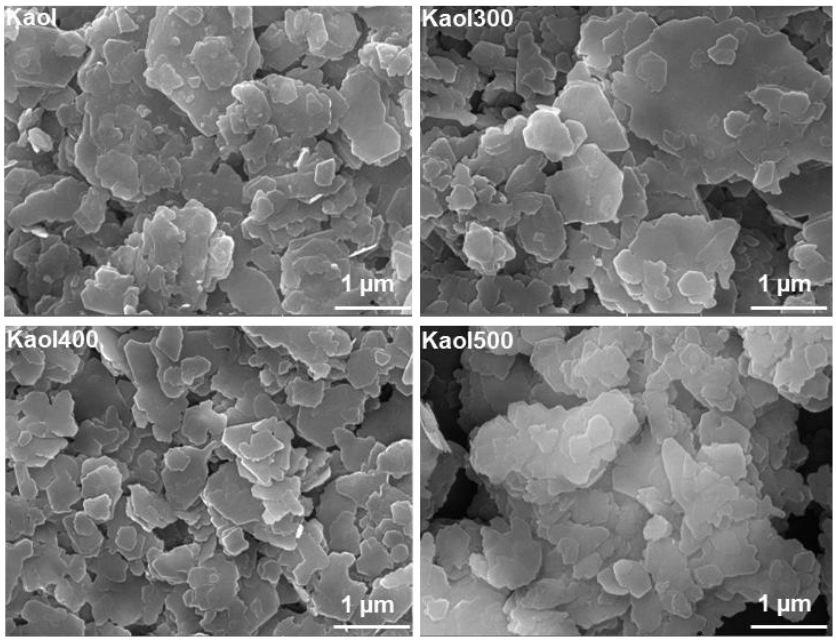

Fig. S2. SEM images of kaolinite samples of different calcined temperature.

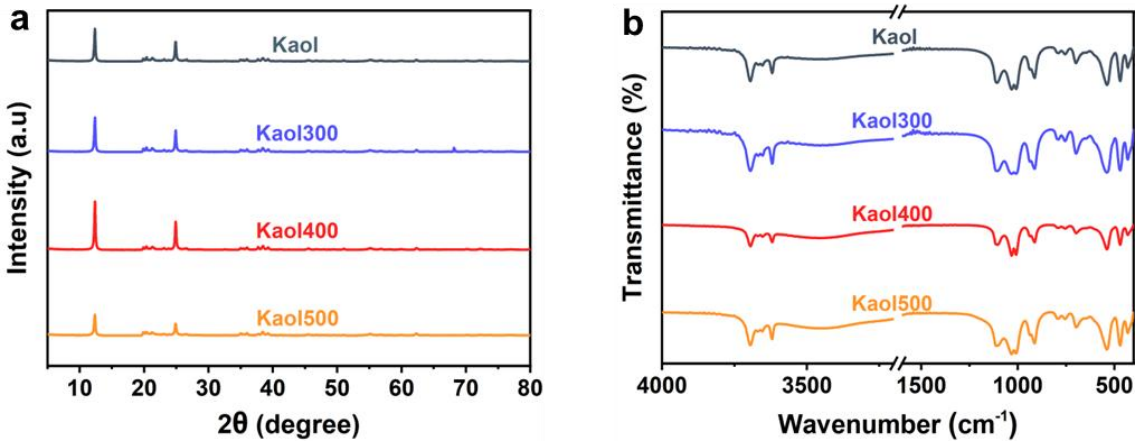

Fig. S3. (a) XRD patterns (b) FTIR spectra of kaolinite samples of different calcined temperature.

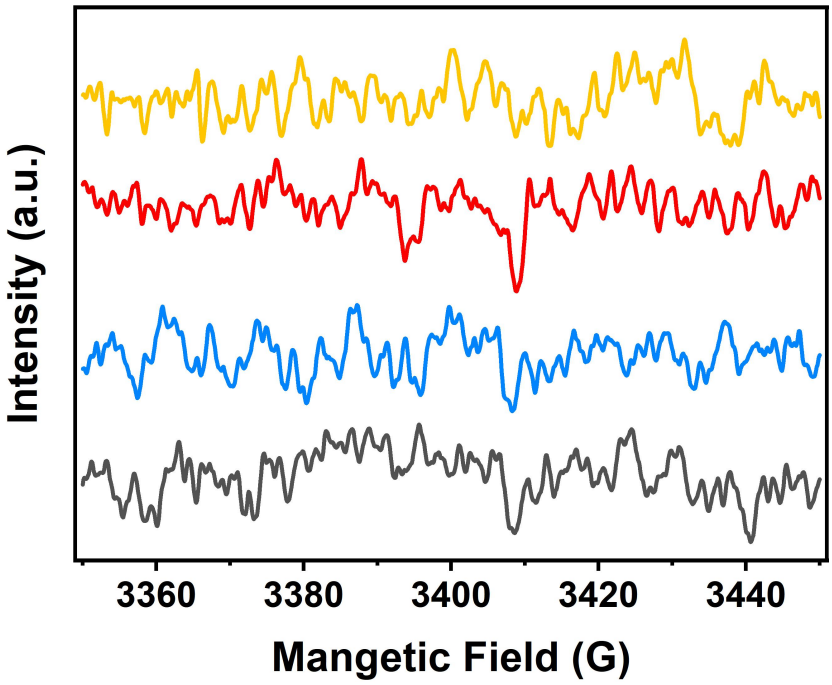

Fig. S4. Hydroxyl and superoxide radical formation of Kaol, Kaol300, Kaol400 and Kaol500.

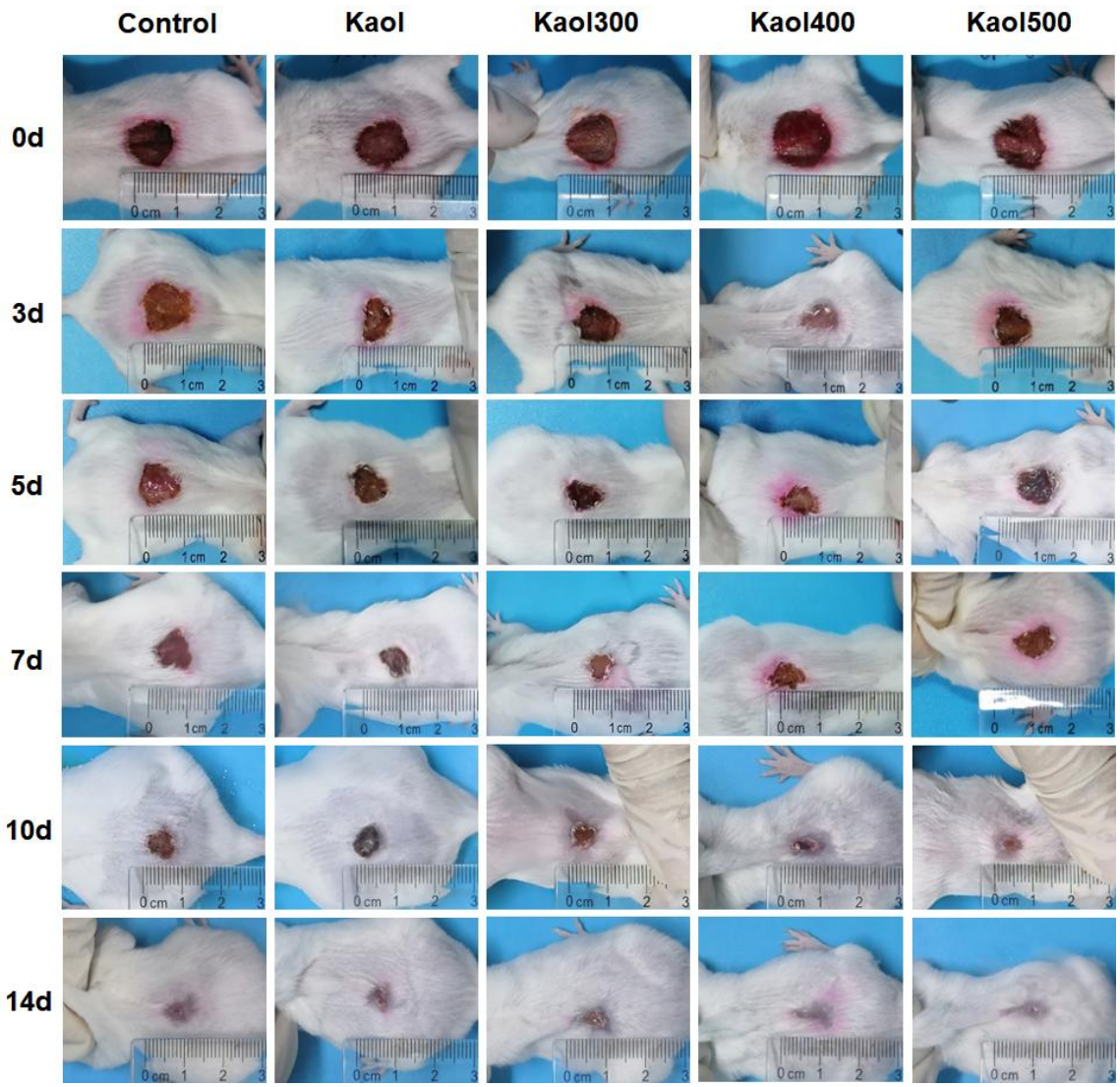

Fig. S5. Representative wound images of wounds in the group.

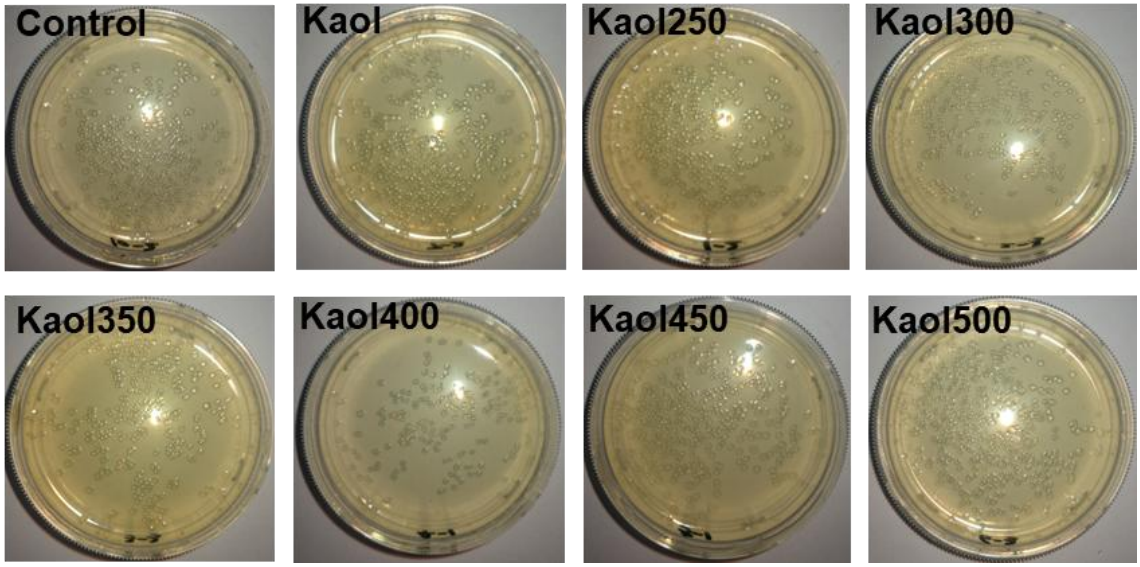

Fig. S6. The corresponding plate colony images after incubation with calcined kaolinite.

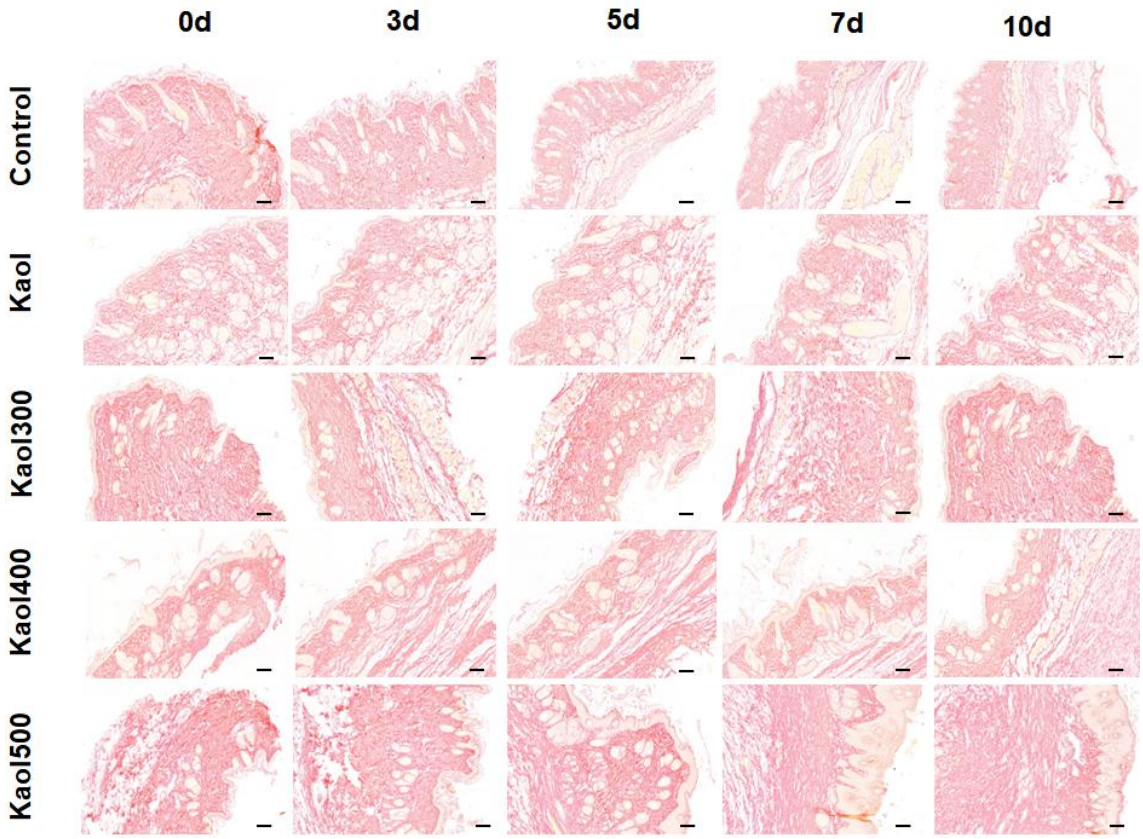

Fig. S7. Sirius red staining on day 0, 3, 5, 7 and 10 of the newly regenerated skin tissues for each group. Scale bar: 200 nm.

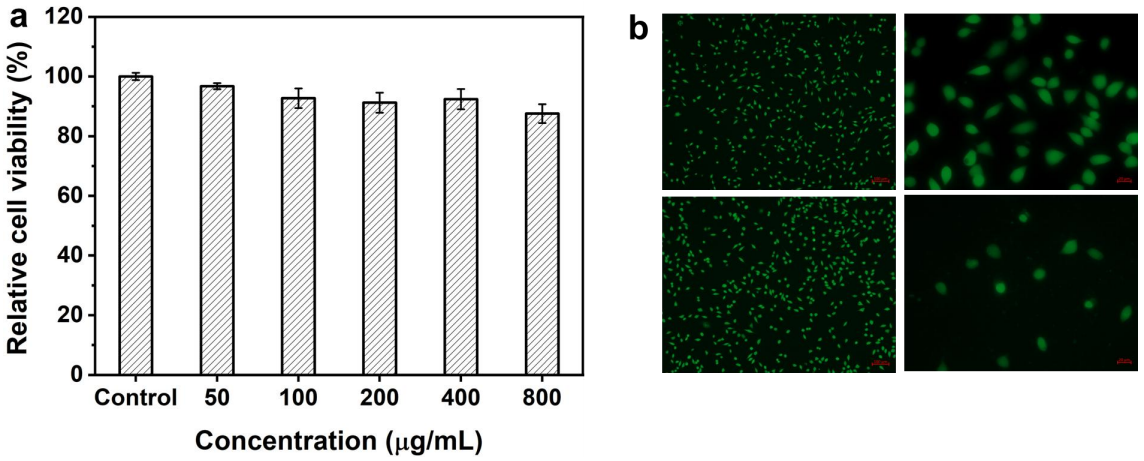

Fig. S8. Cytotoxicity evaluation of samples. (a) Cell viability of kaolinite at different concentrations for 24 h. (b) Live/DEAD staining images of cells after treated with kaolinite and controls (100 μg/ml). (Live cells: green, dead cells: red, scale bar: 100 μm, n = 3).

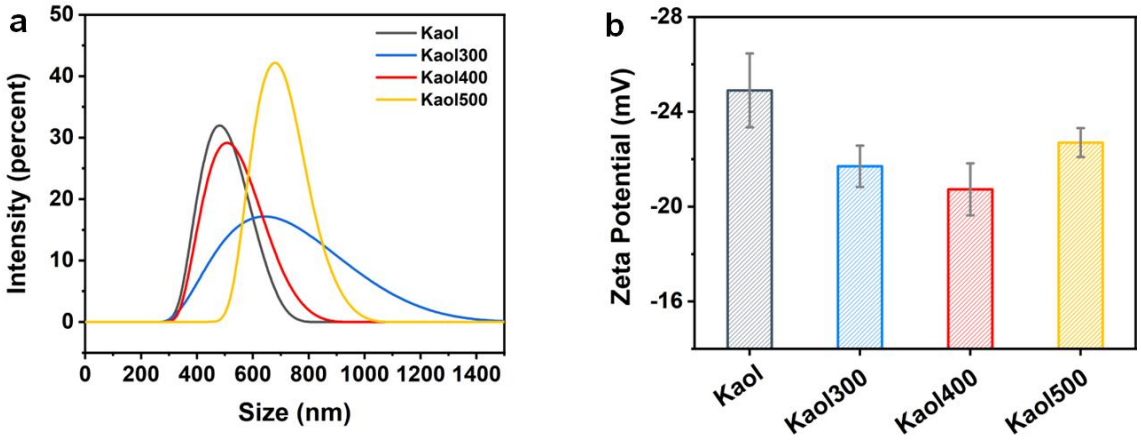

Fig. S9. (a) DLS and (b) Zeta potential values of the calcined kaolinites.

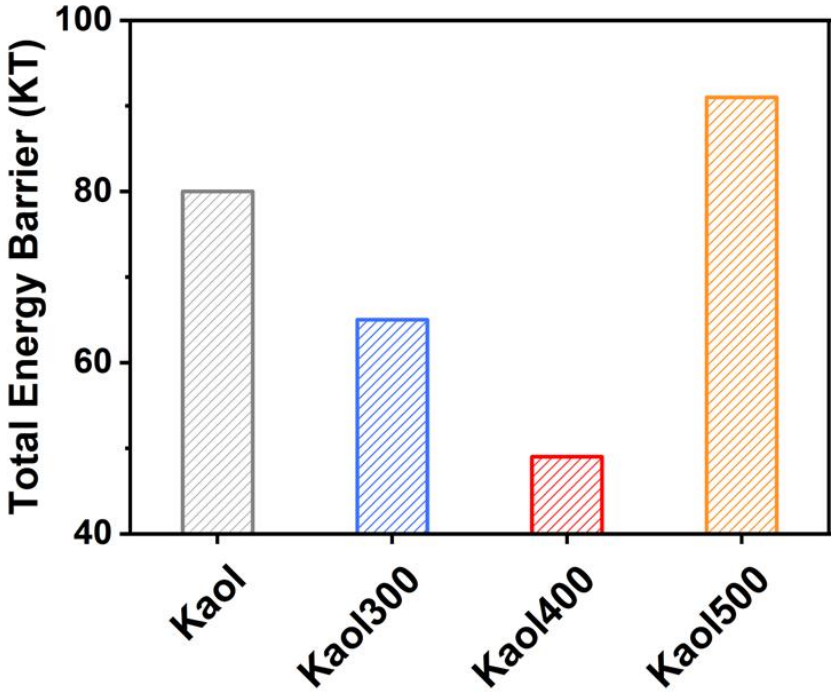

Fig. S10. The total interaction energy barrier between samples and *E. coli*.

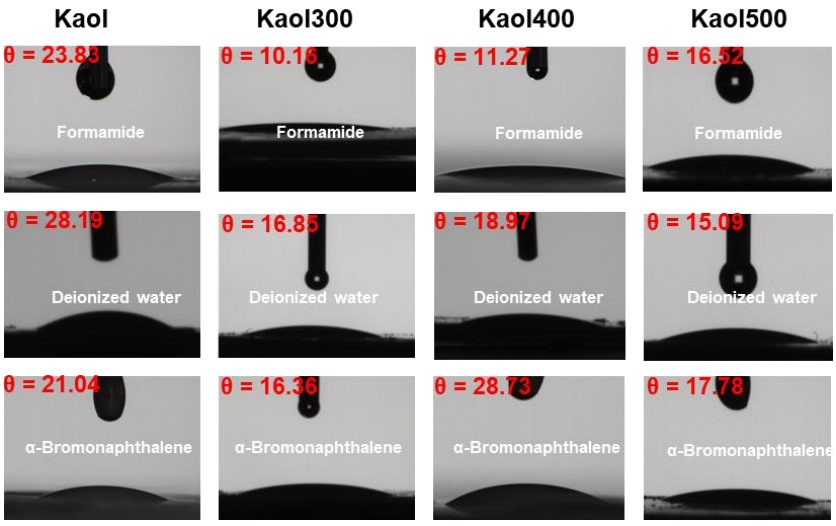

Fig. S11. Contact angles of different liquids for different kaolinite samples.

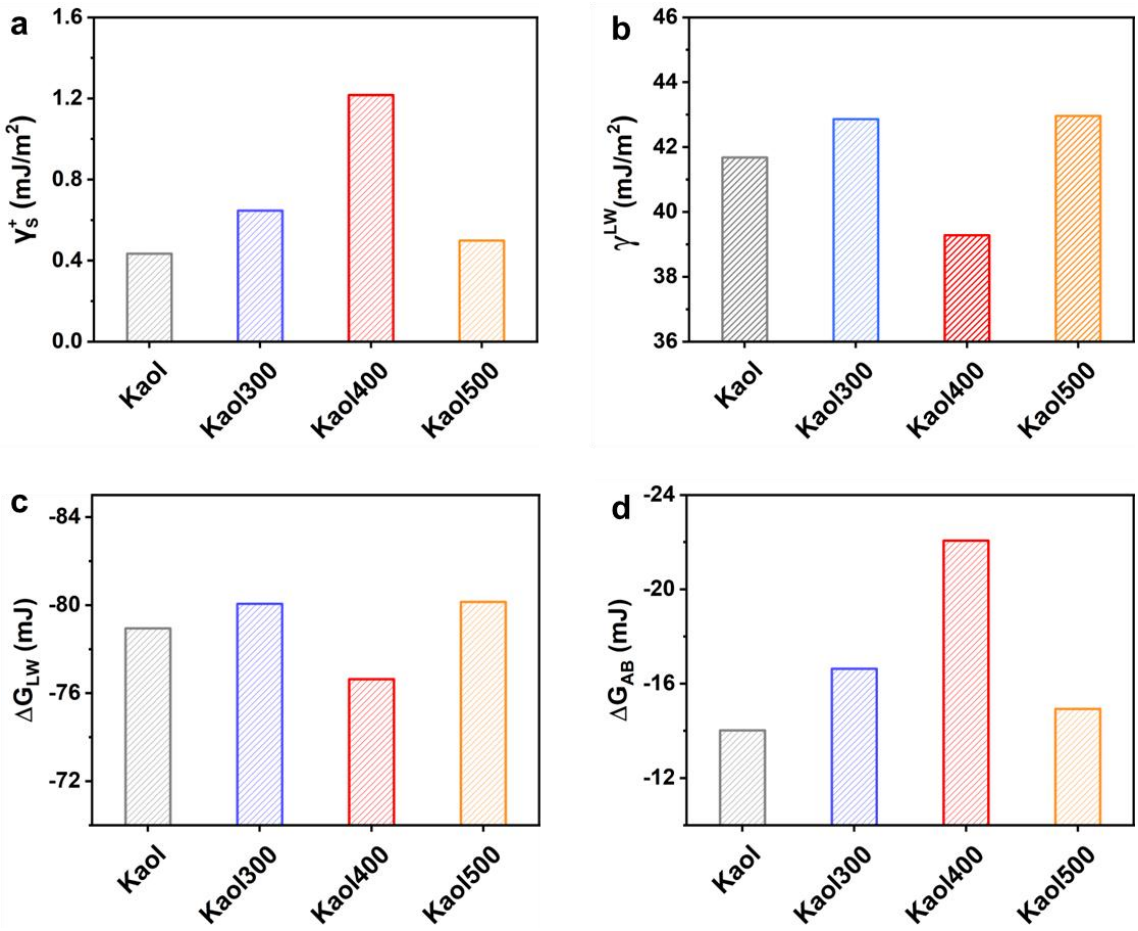

Fig. S12. (a) Lewis acid component. (b) Lifshitz–van der Waals surface free energy. (c) Lifshitz–van der Waals free energy. (d) Lewis acid–base free energy.

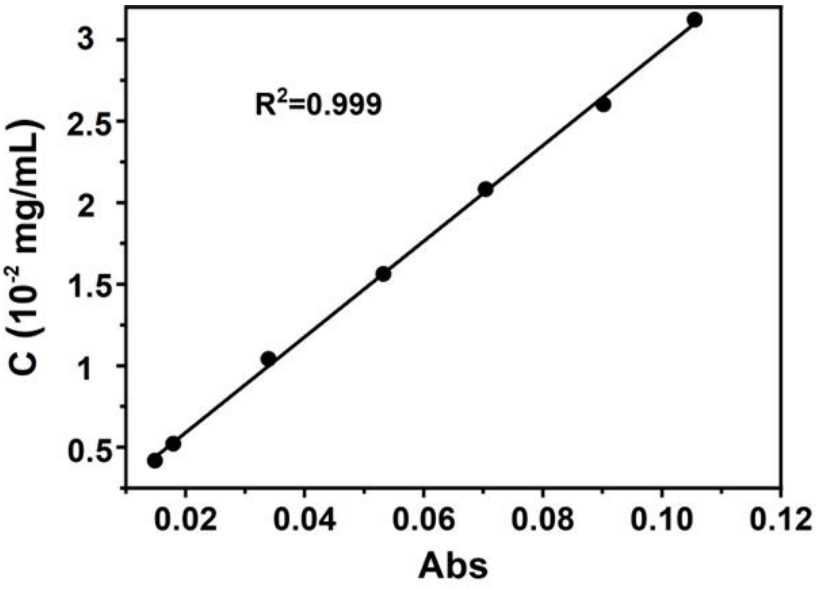

Fig. S13. The standard curve for equilibrium attachment of *E. coli* to samples.

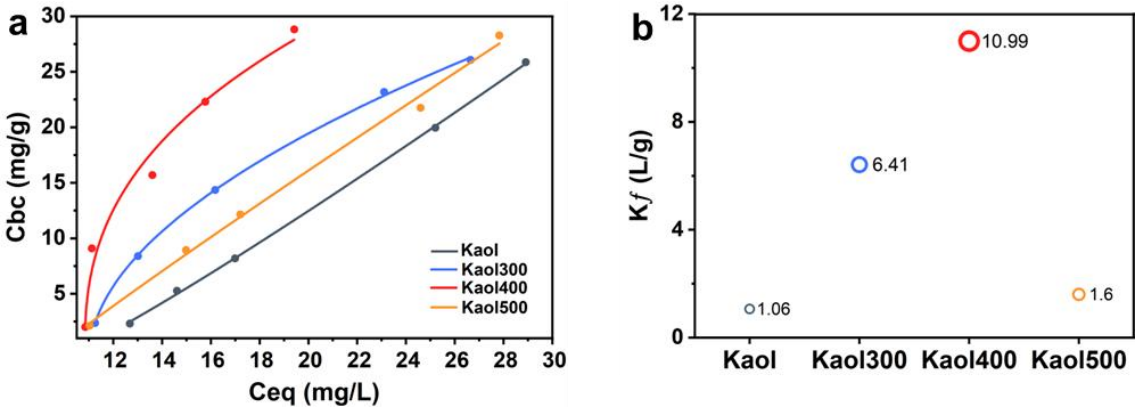

Fig. S14. (a) Fitted curves for attachment. (b) The coefficient of adhesion capacity.

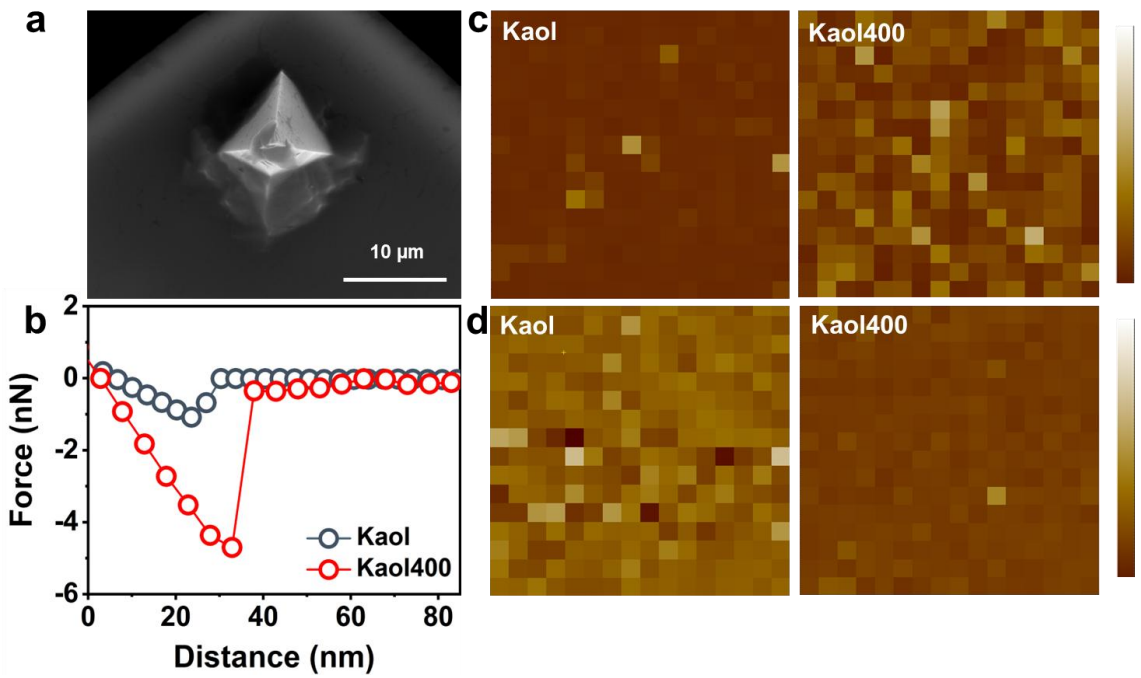

Fig. S15. (a) SEM image of a cantilever with immobilized bacteria. (b) Force-distance curves, (c) interaction force, and (d) interaction energy between *E. coli* and kaolinite.

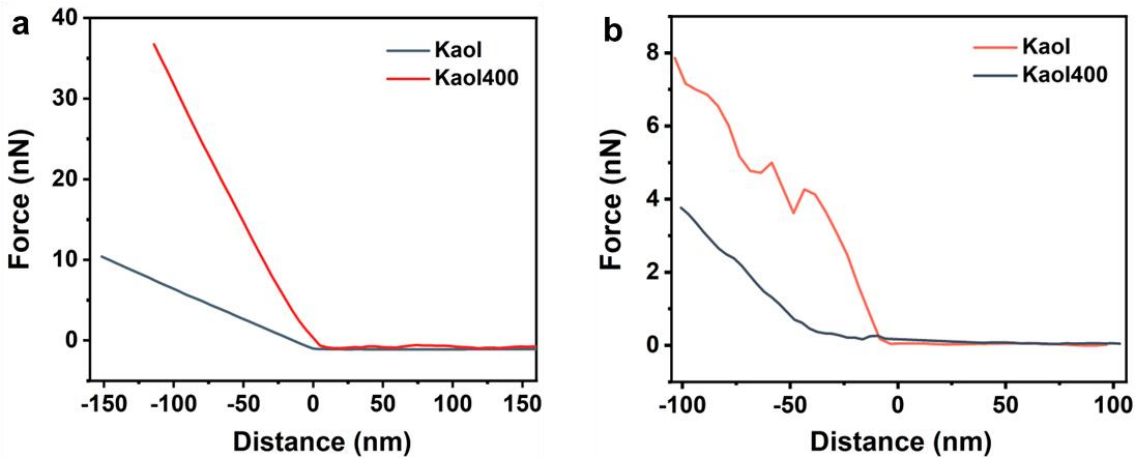

Fig. S16. (a) Extension portion of force curves, and (b) representative extension curves of nonlinear regions between kaolinite and bacteria.

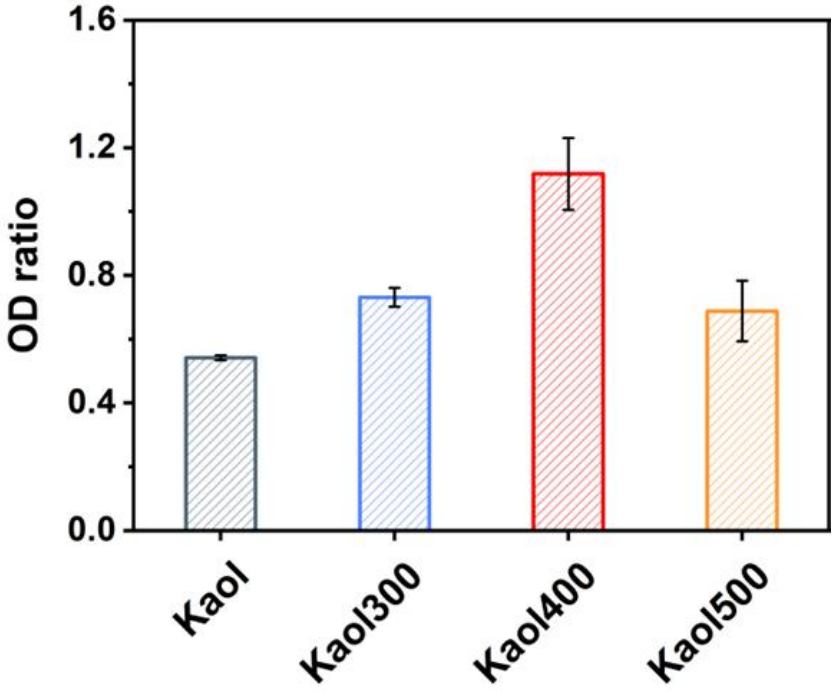

Fig. S17. The release of cytoplasmaic constituents monitored by UV absorption at 260 nm.

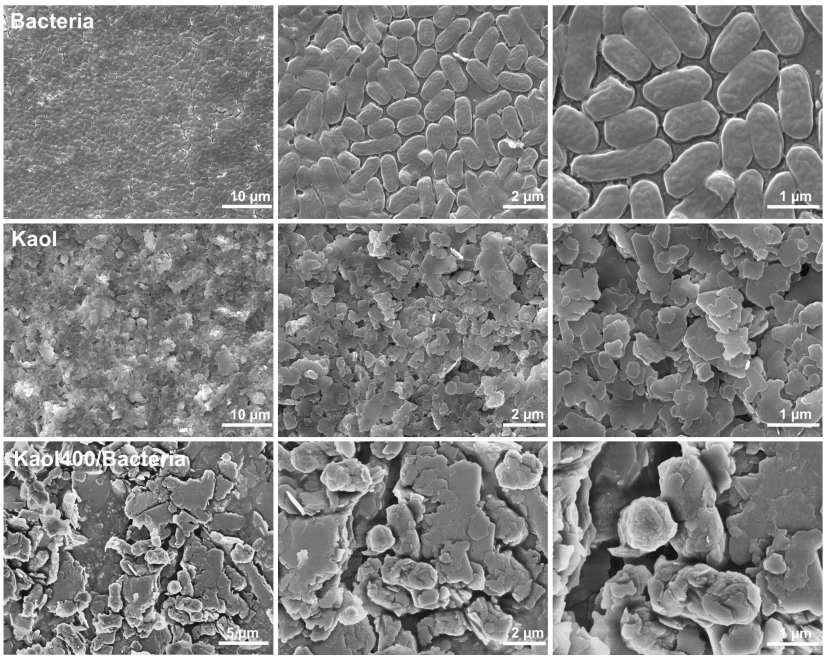

Fig. S18. SEM images of *E. coli.* and *E. coli.* incubated with kaolinite samples.

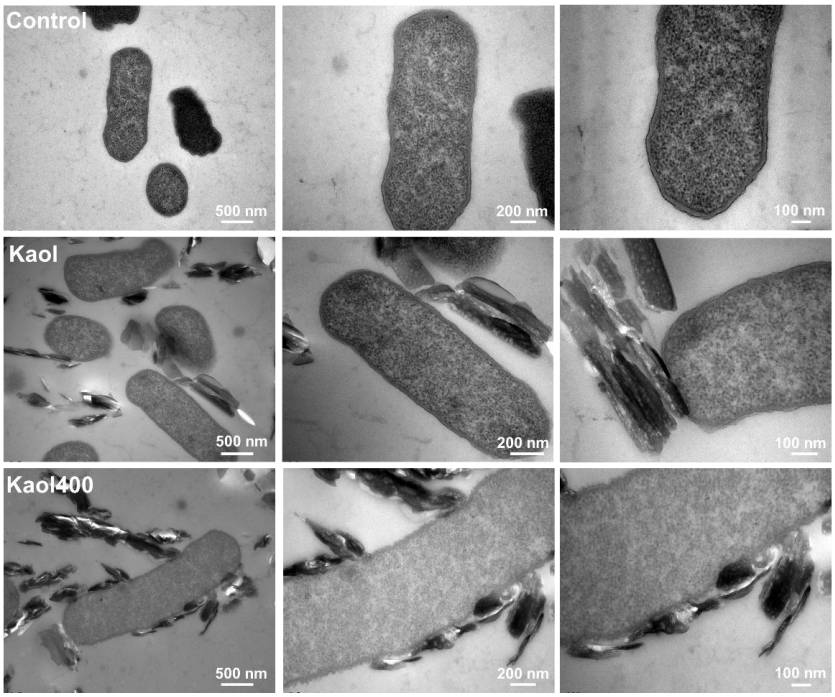

Fig. S19 TEM images of *E. coli.* and *E. coli.* incubated with kaolinite samples.

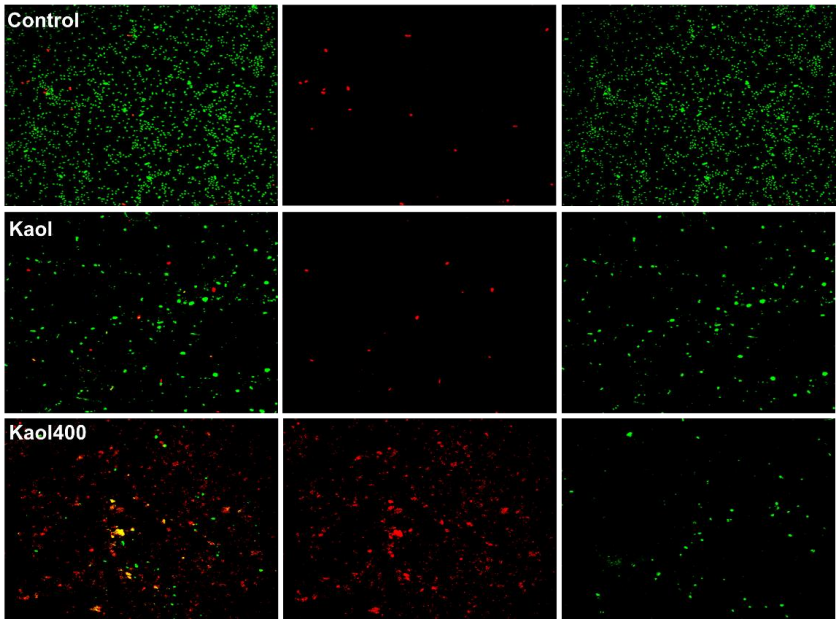

Fig. S20. CLSM images of *E. coli.* and *E. coli.* incubated with kaolinite samples.

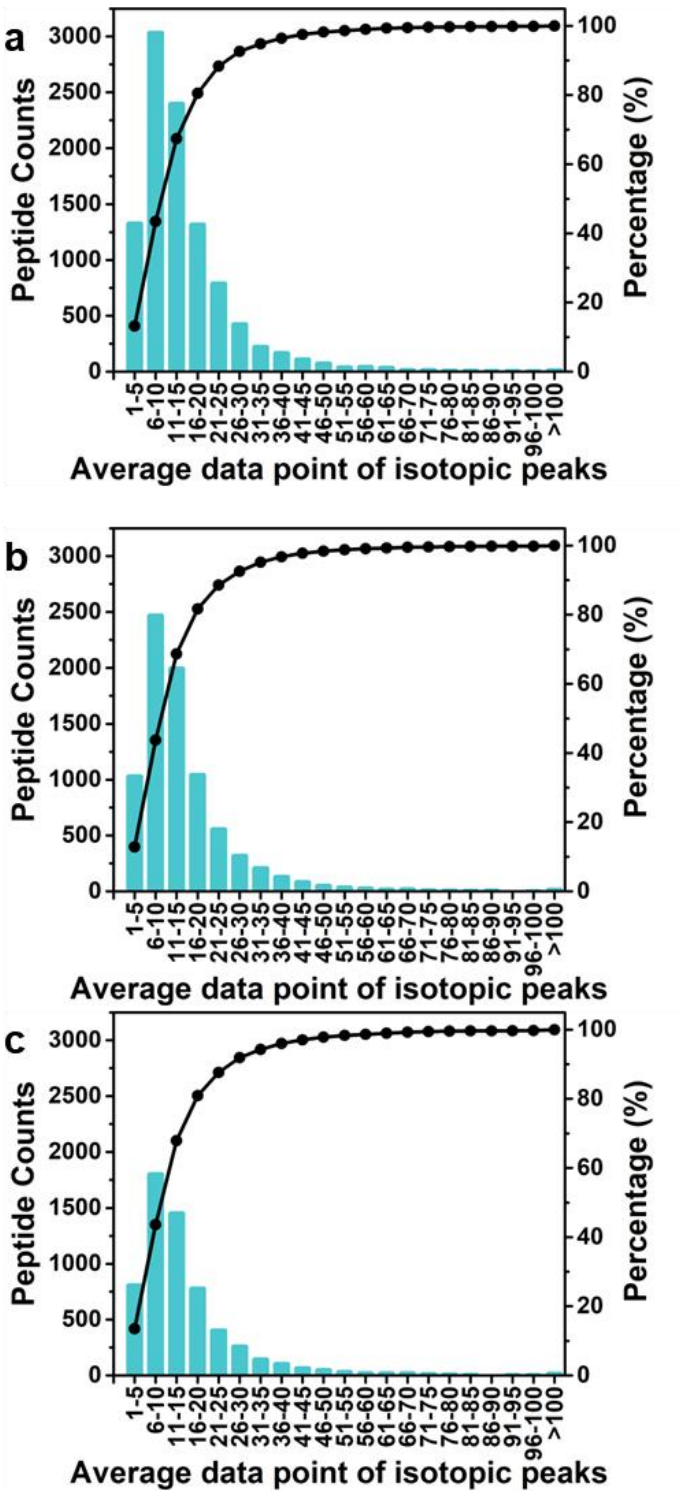

Fig. S21. Peptide data point statistics of exosomes for different samples: (a) The control, (b) Kaol, and (c) Kaol400.

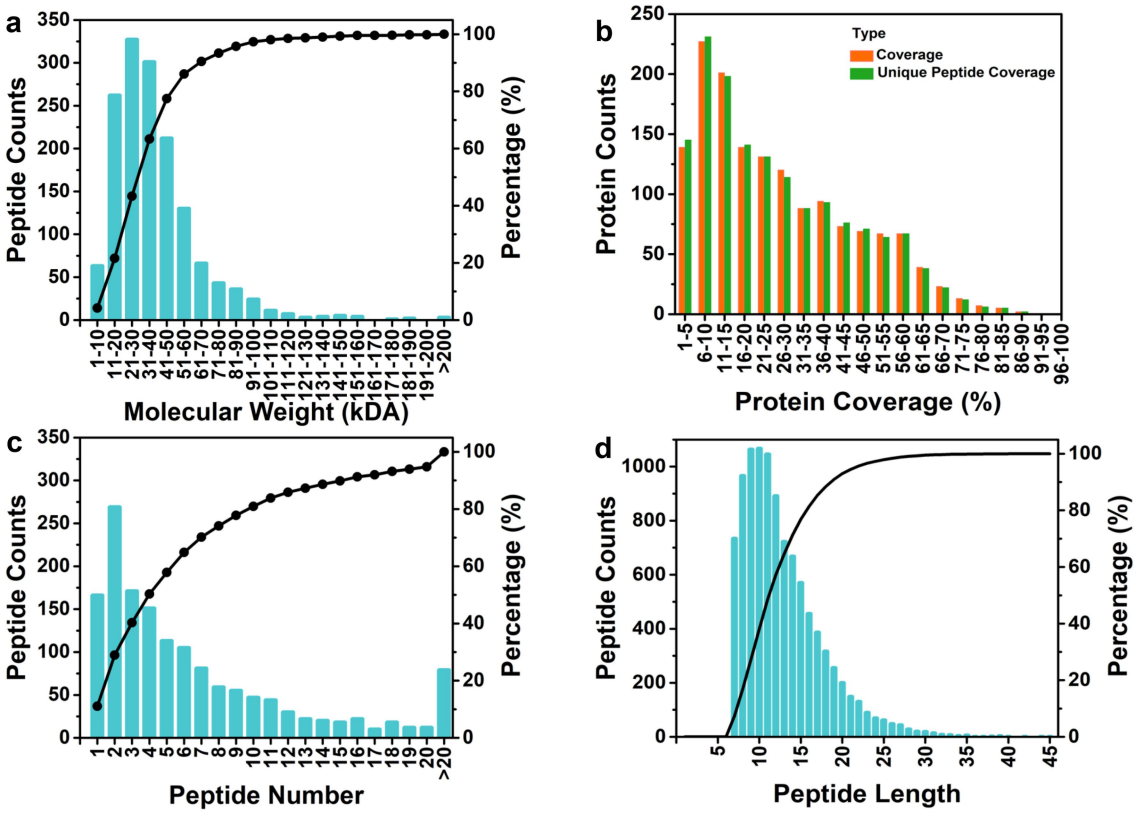

Fig. S22. (a) Molecular weight, (b) Protein coverage, (c) Peptide number, and (d) Peptide length of exosomes.

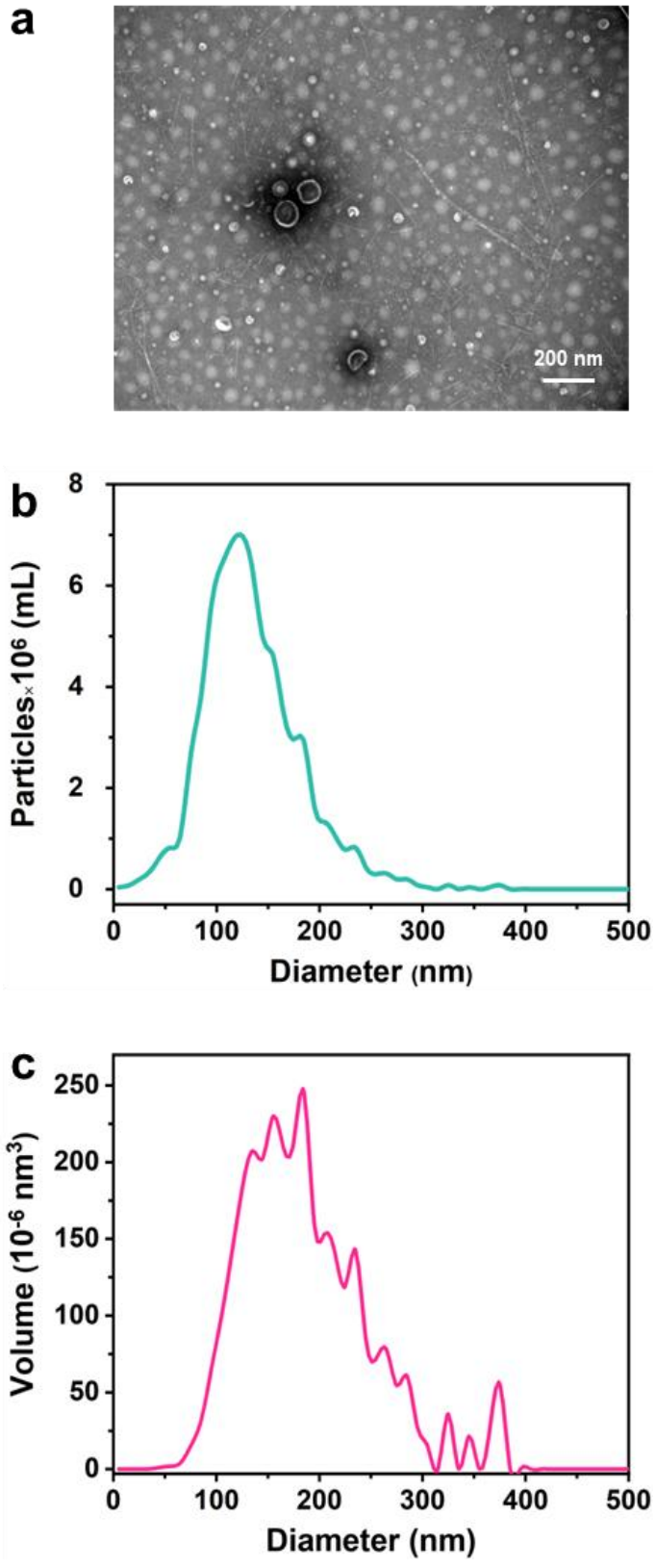

Fig. S23. Exosome properties of bacteria before and after incubation with samples. (a) TEM images, (b) Particle distribution of exosome, and (c) Volume distribution of exosome.

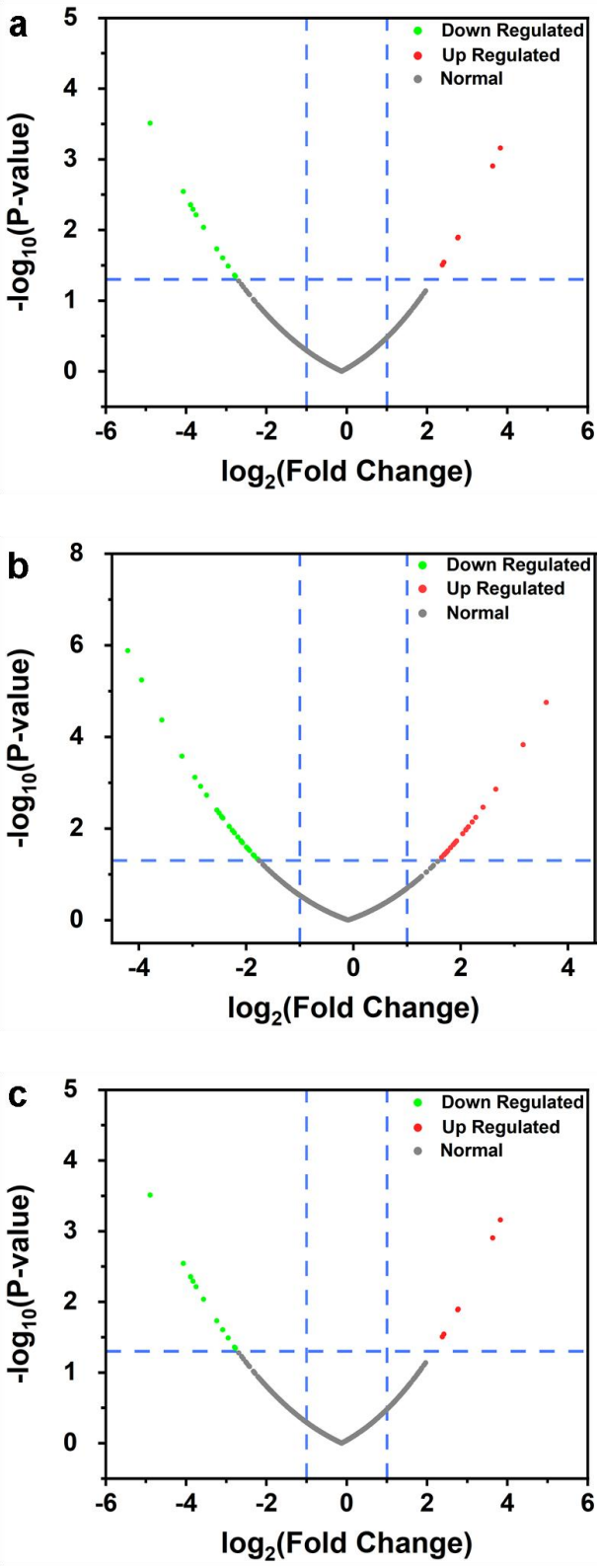

Fig. S24. Volcano plots of differentially expressed proteins for different samples: (a) Control/Kaol, (d) Control/Kaol400, and (c) Kaol/Kaol400.

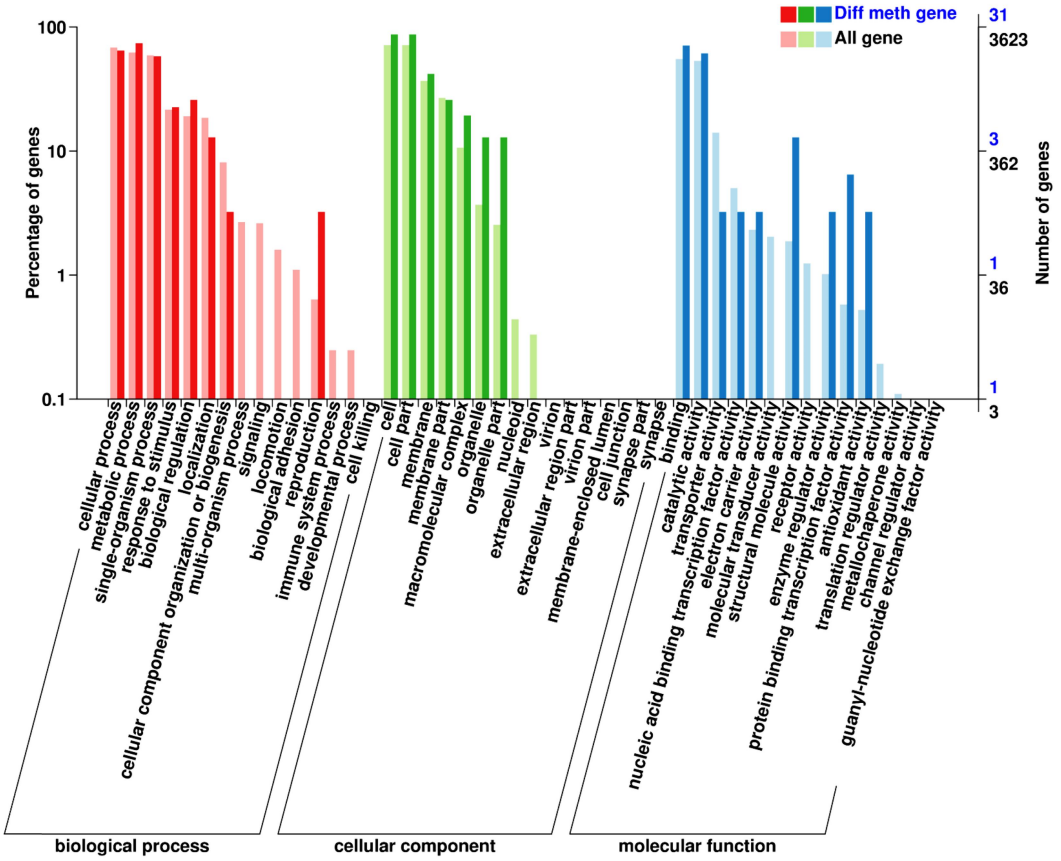

Fig. S25. Differentially expressed proteins of Kaol/Kaol400.

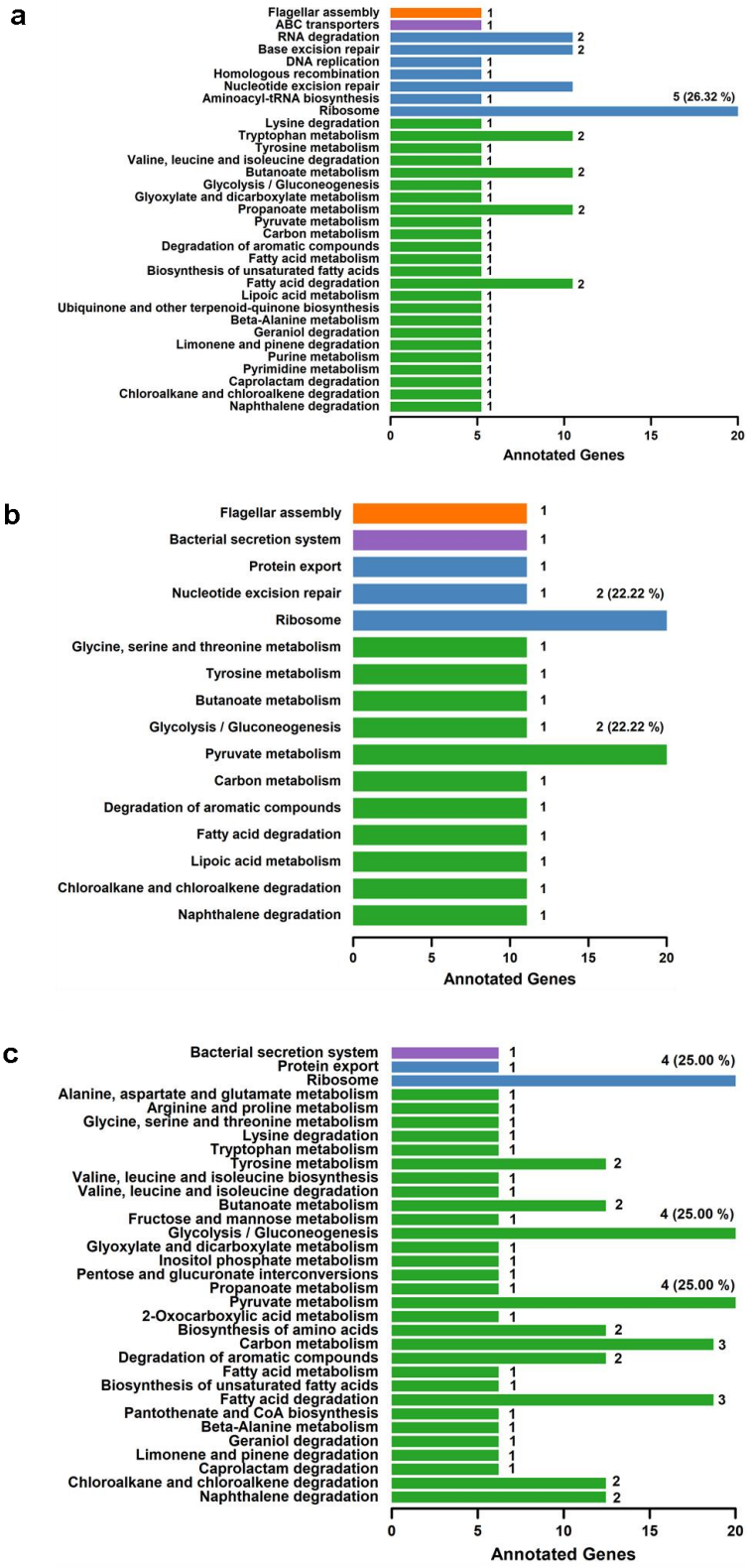

Fig. S26 KEGG classification maps of differentially expressed proteins for different samples: (a) control/Kaol400, (b) control/Kaol and (c) Kaol/Kaol400.

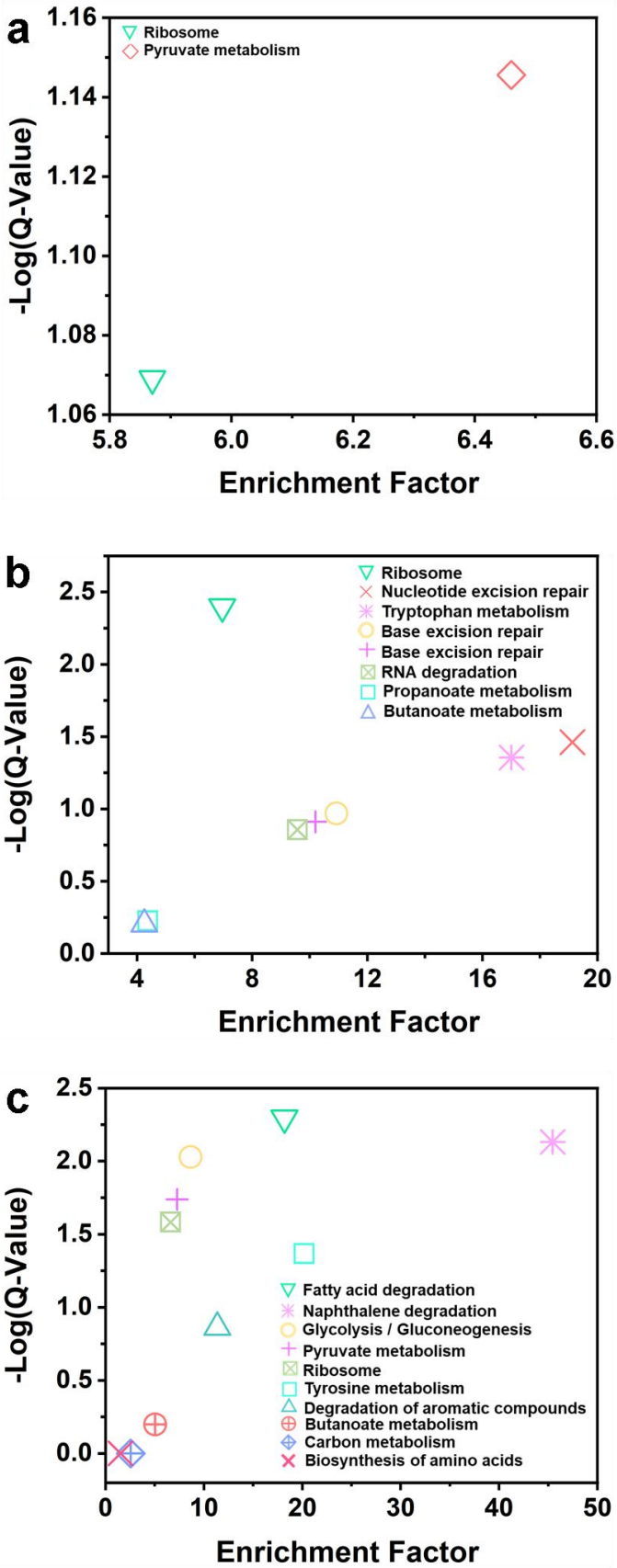

Fig. S27. Enrichment factors of (a) Control/Kaol, (b) Control/Kaol400 and (c) Kaol/Kaol400.

Table S1 Size and zeta potential of samples

Sample	Diameter/μm	Radius/μm	Zeta Potential / mV
Kaolin	0.582	0.291	-24.90
Kaol300	0.816	0.414	-21.70
Kaol400	0.632	0.317	-20.73
Kaol500	1.249	0.637	-22.70

Table S2 Parameters for calculation of DLVO energy

Parameters	Values
Kaolinite refractive index	1.53
Bacterial refractive index	1.55
Water refractive index	1.33
Kaolinite dielectric constant	9.98×10^{-11} $C^2/J\cdot m$
Water dielectric constant	6.95×10^{-10} $C^2/J\cdot m$
Bacterial relative dielectric constant	78.54
Incubate Temperature	37 ℃
Boltzmann constant (κ)	1.381×10^{-23} J/K
Planck constant (*h*)	6.626×10^{-34} J·s
UV-light dominant electron absorption frequency	3×10^{15} s^{-1}

Table S3 The parameters of the surface free energy of liquids

Test liquids	Surface free energy components (mJ/m^2)			
	γ_L^{LW}	γ_L^+	γ_L^-	γ_L
Formamide	39.00	2.28	39.00	54.70
Deionized water	21.80	25.50	25.50	72.80
α-Bromonaphthalene	44.40	0	0	44.40

Table S4 The contact angle data of samples for different liquids

Samples	Formamide	Deionized water	a-Bromonaphthalene
Kaol	23.83±1.87	28.19±2.47	21.04±0.95
Kaol300	10.49±1.72	16.70±1.37	17.44±1.11
Kaol400	10.14±2.50	19.07±0.48	29.07±1.52
Kaol500	16.34±0.95	20.76±2.39	15.65±1.73

Table S5 The parameters of the three-strip model fits to SANS data

Structural parameters	D_c (Å)	D_h (Å)	ρ_C (10^{-5} Å^{-2})	ρ_H (10^{-5} Å^{-2})
Fitted results	92.76	140.22	0.77	0.68

References

1. W. Zhao, S. L. Walker, Q. Huang and P. Cai, *Water Res.*, 2014, **53**, 35-46.
2. S. K. Lower, M. F. Hochella and T. J. Beveridge, *Science*, 2001, **292**, 1360-1363.
3. X. Rong, Q. Huang, X. He, H. Chen, P. Cai and W. Liang, *Colloids Surf. B. Biointerfaces*, 2008, **64**, 49-55.
4. F. A. Heberle, D. Marquardt, M. Doktorova, B. Geier, R. F. Standaert, P. Heftberger, B. Kollmitzer, J. D. Nickels, R. A. Dick, G. W. Feigenson, J. Katsaras, E. London and G. Pabst, *Langmuir*, 2016, **32**, 5195-5200.
5. N. K. Khadka, X. Cheng, C. S. Ho, J. Katsaras and J. Pan, *Biophys. J.*, 2015, **108**, 2492-2501.
6. X. Rong, W. Chen, Q. Huang, P. Cai and W. Liang, *Colloids Surf. B. Biointerfaces*, 2010, **80**, 79-85.
7. F. Eudier, G. Savary, M. Grisel and C. Picard, *Adv. Colloid Interface Sci.*, 2019, **264**, 11-27.
8. J. Jenkins, J. Mantell, C. Neal, A. Gholinia, P. Verkade, A. H. Nobbs and B. Su, *Nat. Commun.*, 2020, **11**, 1626.
9. C. B. Volle, M. A. Ferguson, K. E. Aidala, E. M. Spain and M. E. Nunez, *Colloids Surf. B. Biointerfaces*, 2008, **67**, 32-40.
10. Q. Huang, H. Wu, P. Cai, J. B. Fein and W. Chen, *Sci. Rep.*, 2015, **5**, 16857.
11. G. Wang, S. Jin, X. Ling, Y. Li, Y. Hu, Y. Zhang, Y. Huang, T. Chen, J. Lin, Z. Ning, Y. Meng and X. Li, *Proteomics*, 2019, **19**, e1800274.
12. B. D. Chan, W. Y. Wong, M. M. Lee, W. C. Cho, B. K. Yee, Y. W. Kwan and W. C. Tai, *Proteomics*, 2019, **19**, e1800149.
13. Y. Zhang, F. Liu, Y. Yuan, C. Jin, C. Chang, Y. Zhu, X. Zhang, C. Tian, F. He and J. Wang, *J. Proteome Res.*, 2017, **16**, 170-178.
14. C. Yang, W. B. Guo, W. S. Zhang, J. Bian, J. K. Yang, Q. Z. Zhou, M. K. Chen, W. Peng, T. Qi, C. Y. Wang and C. D. Liu, *Andrology*, 2017, **5**, 1007-1015.
15. R. J. Simpson, S. S. Jensen and J. W. Lim, *Proteomics*, 2008, **8**, 4083-4099.